Development and Optimization of Micro-Nanotopographical Platforms for Surface Enhanced Raman Scattering Biomolecular Detection

Odetade, David Femi; Rickard, Jonathan J. S.; Goldberg Oppenheimer, Pola

DOI:
10.1002/admi.202400352

Document Version
Publisher's PDF, also known as Version of record

Citation for published version (Harvard):
Odetade, DF, Rickard, JJS & Goldberg Oppenheimer, P 2024, 'Development and Optimization of Micro-Nanotopographical Platforms for Surface Enhanced Raman Scattering Biomolecular Detection', *Advanced Materials Interfaces*. https://doi.org/10.1002/admi.202400352

ADVANCED MATERIALS INTERFACES
Open Access
www.advmatinterfaces.de

Development and Optimization of Micro-Nanotopographical Platforms for Surface Enhanced Raman Scattering Biomolecular Detection

*David Femi Odetade, Jonathan J. S. Rickard, and Pola Goldberg Oppenheimer**

Topologically designed micro- and nanostructured surface-enhanced Raman scattering (SERS) substrates propel the advancements of innovative applications, including environmental and forensic point-of-care miniaturised devices via enhancing the localised electric fields for accurate analyte sensing. Herein, a method for designing, optimising and fabricating fine-tuneable concentric hexagonal, triangular and rectangular SERS-active micronano-substrates is developed, with each unit yielding significant enhancement. Numerical simulations of the 3D near-field electric field guided the optimal design process. While the coaxial SERS substrates consistently outperformed their solid counterparts, the hexagonal micro-nano topologies exhibited ×21 higher signal than coaxial square arrays and a 12-15-fold increase over the triangle structures. Alternation of the topological designs from square to triangle lattice yielded more uniform plasmonic modes propagating along the 60°-directions with various resonance modes playing key roles in light reflectance. This enables the engineering of platforms with tailor-enhanced signals by changing the arrangement of micro-nano patterned coaxial arrays. The fabricated SERS substrates are validated by detecting traumatic brain injury biomarkers, effectively yielding the characteristic fingerprint spectra of each neuro-molecule. The straightforward development of sub-micrometre tuneable SERS-active architectures enables anelegant route for high-throughput biochemical sensing, laying a platform for amplified bimolecular detection of disease biomarkers and integration in bioanalytical systems.

1. Introduction

Surface-enhanced Raman spectroscopy is a highly sensitive spectroscopic and rapid sensing technique, enabling detection down to single molecule levels.[1,2] In the past decades, SERS has emerged as a powerful analytical tool for a breadth of applications. It is particularly ubiquitous in medical diagnostics[3–12] due to its unique ability to detect *trace-level* concentrations of disease-indicative biomarkers without specific antibodies, labeling or requiring complex sample preparation. It is also one of the not many spectroscopic techniques, which enables the ability to be deployed out of the laboratory settings without significant loss in performance. While high-enhancement is possible using metallic nanoparticles, due to their poor batch-to-batch reproducibility, only a minute fraction of these exhibit the desired SERS-activity, i.e., consistent "hot-spots". This substantially affects the achievable signals and sensitivity.[13–17]

The substrate on which SERS is performed is often the critical component for successful, consistent, and reproducible detection[18–22] Sub-microstructured SERS substrates have been evolving, however, the micro- and nano texturing of plasmonic structures inside micro-devices remains challenging and complicated, especially for low-cost fabrication. Most synthetic routes to generate SERS structures are based on conventional photolithographic techniques. These are costly, time-consuming, cumbersome, and require precise integration of multi-step processes,[23–32] thus, limiting the

D. F. Odetade
Centre for Doctoral Training in Topological Design
School of Physics and Astronomy
University of Birmingham
Birmingham B15 2TT, UK

The ORCID identification number(s) for the author(s) of this article can be found under https://doi.org/10.1002/admi.202400352

DOI: 10.1002/admi.202400352

D. F. Odetade, J. J. S. Rickard, P. Goldberg Oppenheimer
School of Chemical Engineering
College of Engineering and Physical Science
University of Birmingham
Birmingham B15 2TT, UK
E-mail: goldberp@bham.ac.uk

J. J. S. Rickard
Department of Physics
Cavendish Laboratory
University of Cambridge
JJ Thomson Avenue, Cambridge CB3 0HE, UK

P. Goldberg Oppenheimer
Institute of Healthcare Technologies
Institute of Translational Medicine
Mindelsohn Way, Birmingham B15 2TH, UK

scalability of the resulting SERS substrates. The limited resolution, inevitable defects, poor mechanical stability of the mold, and pattern distortion are the further limiting factors of the employed lithographic techniques. The precise control of features, prevention of defects and reproducibility, therefore, remain a challenge, particularly in the sub-micrometer regimes.

A considerable signal enhancement in SERS is typically achieved via the designed and fabricated metallic surface micro-nano topologies[33–35] arising from the surface plasmons, which are collective oscillations of electrons on the metallic surfaces, excitable by the incident light.[36,37] These yield an increased electric field near the surface of the metallic structures, which interacts with the target molecules, effectively augmenting the Raman scattering signal. The SERS enhancement factor is dependent on the local electric field enhanced at both the incident frequency ($E_{\text{Incident}}{}^2$) as well as the Raman scattered ($E_{\text{Scatettered}}{}^2$) frequency, resulting in an overall E^4 electromagnetic enhancement. Hence, the overall enhancement is maximized when surface plasmon resonances are generated at both the frequencies of the in-going and outcoming photons, leading to high SERS signals.[38,39] Lithographically defined, periodic SERS substrates typically sacrifice a degree of sensitivity due to larger surface features. Nevertheless, these enable better spot-to-spot uniformity for a given sample and higher reproducibility across multiple samples. The design and fabrication of the optimal structures are typically focused on achieving more consistent substrates. These comprise reproducible areas of significant local electric field enhancement, i.e., the "hot spot" to improve the accuracy and analytical sensitivity of detection.

Slight topological changes via tunable parameters in SERS designs play an important role in the enhancement of the Raman signals produced. However, various techniques for fabricating SERS-active substrates capable of fulfilling a multitude of criteria remain challenging. For instance, despite a larger number of hotspots, nanorods and nanowires require advanced and cumbersome fabrication techniques.[39–41] Metallic solid nano-pillars, whilst exhibiting high enhancement and consistency, are often insensitive to spatial orders and periodicity variations.[42] Ring cavity-enclosed bimetallic SERS "nano stars" fabricated via electron beam lithography have been shown to provide good control of hotspot location and homogeneity. However, these are time-consuming and the typical fabrication of $\approx cm^2$ area with dimensions in the 20 nm range takes several days to complete. It is also of a high-cost and requires trained specialist personnel, limiting the scalability of such substrates.[43–46] The choice of surface metal is also dictated by the plasmon resonance frequency. Whilst silver constitutes a common metal for SERS substrate production, it is highly prone to oxidation in air. Gold-based structures, on the other hand, are more biocompatible and less toxic, providing large enhancements, chemical robustness, biocompatibility, and straightforward functionalization chemistry.[47–53] Recently, coaxial metallic micro and nano-architectures have been gaining popularity as SERS-active structures due to the increased tunability through the topological design alterations. This allows various engineering shapes and sizes as well as the fabrication of larger hot spot areas thus, enabling a larger number of molecules to attach in these regions.[54] The control of wall thickness in concentric metallic structures is crucial in achieving optimal resonance effects, which can be fine-tuned to match the excitation wavelength and optimize SERS enhancement.[53–55] These architectures also allow the modification of the sharpness of the resonance curve, increasing the achievable SERS intensity at the Raman wavelengths near the resonance.

Herein, lithographically defined concentric micro- and nanostructures were systematically designed and fabricated as reproducible arrays for SERS. These were subsequently tested for their performance as analytical substrates and validated for proof-of-concept detection of neurological biomarkers. For achieving the optimal signal enhancements of the to-be-fabricated topologically structured platforms, the various morphologies were simulated via 2D and 3D near-field electric field distribution. This revealed the predominant localization of the enhanced electromagnetic fields within the noble metal micro-nanostructures, which guided the fabrication of the SERS substrates. These included concentric and solid hexagonal, triangular and rectangular morphologies with increased surface area and hot spots. In turn, it enables a larger number of molecule interactions in each region and a broader bandwidth, yielding augmented SERS signal intensity. The fabricated substrates were tested for detection of four representative brain-specific biomolecules released during cellular damage, which are complementary indicators for diagnosing traumatic brain injury (TBI) and assessing its severity. These included: (i) sphingomyelin, which is known for brain myelination and regulation of inflammatory response vital in the regulation of cellular growth rate, differentiation and cell death in the central nervous system;[56] (ii) S100B, a calcium-binding protein synthesized in glial cell subtype, which modulates long-term synaptic plasticity;[57] (iii) myoinositol, a sugar-derivative produced in glial cells found to be elevated in proportion to the severity of TBI, which also regulates the glial and neuronal activity and intracellular [Ca^{2+}] as well as participates in intracellular signaling pathways;[58] and (iv) cholesterol, a key component of the cellular membrane, known to increase due to the cellular damage, building up following dysregulation and causing cellular toxicity.[59]

Overall, the ease of fabrication and scalability of these structures could enable tunable engineering of a broad range of SERS-active topological designs, including, for instance, concentric nanowells and nanopillars. These, combined with the flexibility of plasmonic metal selection, allow the optical properties and surface chemistry to be tailored for excitation laser, signal enhancement and specific applications.[20,60,61] The developed topological surfaces structured on micro and nanoscales further lay the platform for achieving improved sensing capabilities, which in the longer term, can be integrated into miniaturized lab-on-a-chip technologies.

2. Results and Discussion

An array of concentric topological substrate designs with a range of geometries, including hexagonal, triangular, and rectangular coaxial architectures, were modeled and optimized via COMSOL simulations (**Figure 1**) and CAD Autodesk Fusion-360 (**Figure 2d–f**), respectively. The simulated maximum achievable local electric field enhancement for each metallic structure is shown in Figure 2h. The numerical calculations were carried out in COMSOL using a plane wave illumination to model the incident laser light. This wave had a transverse field component

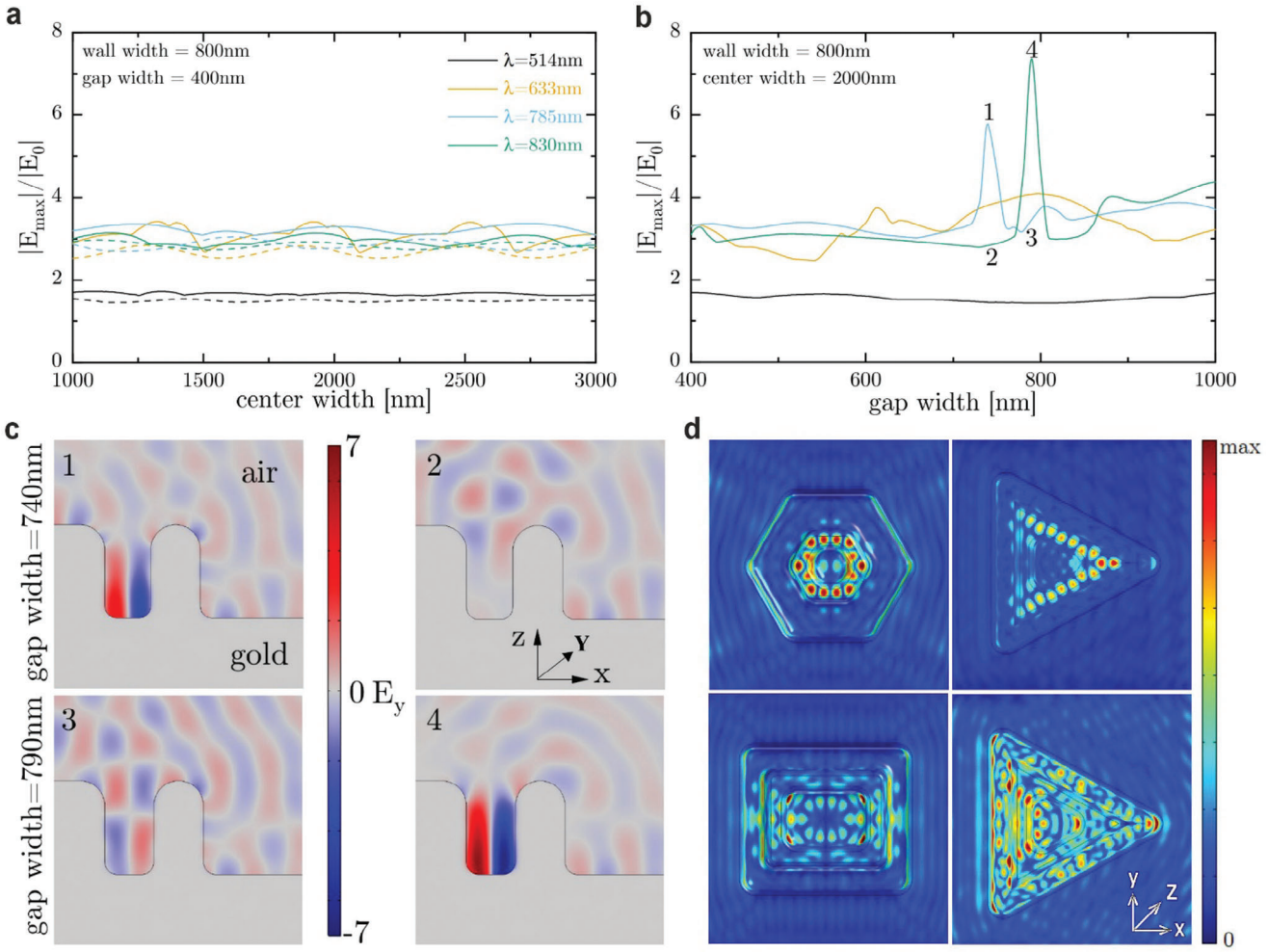

Figure 1. a) Maximum field enhancement of 2D concentric structures (solid lines) and solid structures (dashed lines) with varying width of center. b) Maximum field enhancement of 2D concentric structures versus the gap width. The simulations were carried out for *x* and *y* polarized incident waves and the maximum value of the field on the surface of the structure was taken. c) Electric field profile of 2D concentric structures for the 785 nm (left) and the 830 nm (right) excitation wavelengths with the (c, 2) incoming wave propagating in *z* direction, the electric field polarized along the *x* direction and the magnetic field polarized in the *y* direction. d) 3D near-field simulations of the electric field distribution for hexagonal (650 nm gap), square (800 nm gap) and triangle (750 nm gap) coaxial micronano-structures with the visible confined and scattered field components for 785 nm (left column and bottom row) and 830 nm (top right) excitation. The incoming wave is propagating in *z* direction, the electric field is polarized along *x* direction and the magnetic field is polarized in *y* direction.

to the direction of propagation (*z*-axis) with the relative permittivity of *Au* as a function of λ. The designed arrays of concentric topological hexagonal, triangular, and rectangular substrates were systematically analyzed for a range of inner and outer diameters, gap and wall widths and periodicity. These revealed that the relative enhancement correlates with the gap-to-width parameters (Figure 1), allowing to optimize and guide the subsequent SERS substrates fabrication.

To study the SERS response of the fabricated coaxial micronano-structured substrates, the variation of peak wavelength resonance and the intensity enhancement for the resonance as a function of gap width in the concentric arrays, the generated E_f of the gold-coated arcatures was numerically simulated via a 3D model. A finite-element method was implemented where a plane wave is incident normal to the substrate with a linear polarization perpendicular to the top edge, with the simulation being infinite in the third lateral direction (i.e., infinite ridges with cross-sections).

Since the full 3D simulations for the larger micro-nano structures are computationally expensive, the dependence of the maximum field enhancement with the center, gap and wall widths was investigated using simplified 2D topologies (Figure 1a–c). Here, a 400 nm edge rounding was applied at the top (for 2D and 3D) and on the side (for 3D) micro nanostructures and a 200 nm edge rounding at the bottom (limited by other geometric parameters). This collectively enabled removing the edge impacts and highlighting the cavity effects. For the solid structures without an external wall, the center width has a negligible effect (Figure 1a) since the plasmons are excited along the sides and propagate away from the structure, which is independent of the center width in this parameter range. For the concentric structures (Figure 1a), the effect is also minimal. However, it is

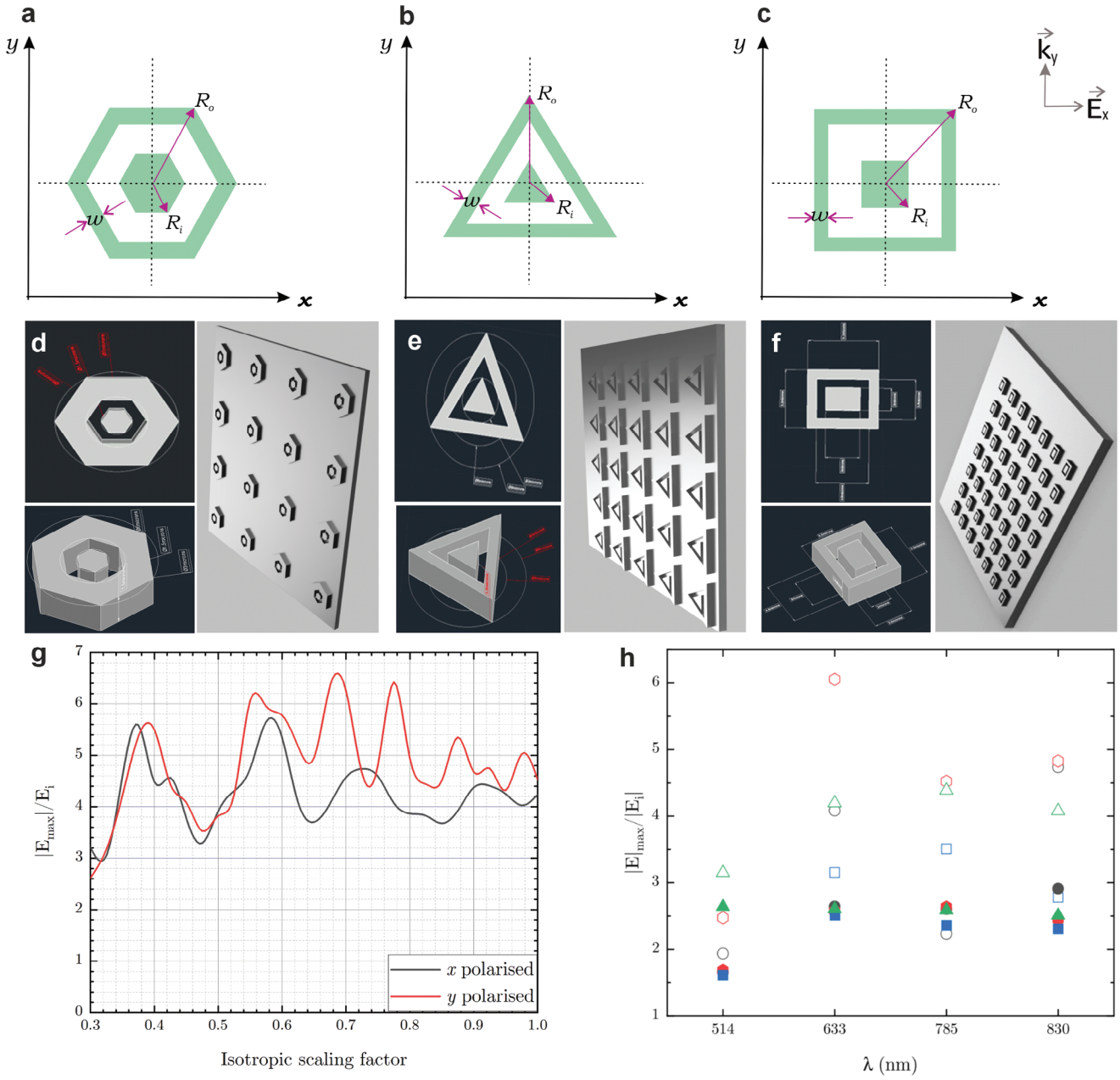

Figure 2. Concentric topological substrate design for SERS including a) hexagonal, b) triangular and c) rectangular geometries inscribed in the three circles (for hexagonal and triangular), with the d–f) corresponding CAD and Fusion 360 designs top view (top left) and 3D view (bottom left) and 3D periodic arrays (right-hand side). g) Maximum calculated field enhancement under isotropic scaling for *x* and *y* polarized excitation. h) Comparison of the theoretical simulated maximum achievable field enhancement for each metallic structure, including the concentric hexagonal, rectangular, and triangular and their corresponding solid counterparts at excitation wavelengths of 514, 633, 785, and 830 nm, where $|E|_{max}$ calculated for *x* and *y* polarized plane wave.

found to be more prominent, most probably due to the plasmons launching on the inner side of the wall, subsequently propagating across the center and interfering. Similarly, varying the wall width exhibited an even smaller effect on the concentric micronanostructures. From 2D simulations, the maximum field enhancement for the fabricated concentric structures was found to be most sensitive to the gap width parameter (Figure 1b,c). From a modal perspective, this parameter determines the formation of the localized plasmon mode at the bottom of the well. From the excitation perspective, it determines which wavelength couples most efficiently to the plasmon. While both 785 and 830 nm excitation wavelengths exhibit a strong and narrow resonance peak, these are found at different gap widths. The 633 nm laser outperformed these for a wide variety of gap widths, albeit with the maximum achievable field enhancement being lower than for the other two excitation lasers (Figure 1b). From the electric field

profiles for the 785 and the 830 nm excitation wavelengths, high-quality localized plasmon mode is evident for the 740 nm and 790 nm gap width, respectively (Figure 1c). When the gap width or excitation differ from these, the coupling strength is reduced, and other modes are excited. This effect also leads to the 633 nm excitation having an overall good performance across a wide parameter range (i.e., 600–850 nm), with the maximum achievable enhancement, however, lower than for 785 or 830 nm lasers. The 514 nm excitation demonstrates a poor enhancement across all scenarios due to the combination of a small refractive index and large extinction coefficient of gold at this wavelength, with the cavity not supporting a localized high-quality mode as such frequencies. This highlights the gap width as a key parameter for the design of optimized coaxial SERS-active substrates whilst indicating the detailed structural properties coming into play for optimized EFs.

3D near-field simulations of the electric field distribution (Figure 1d) exhibit the highest EF at 785 nm excitation (left column and bottom row) for the triangular architecture, correlating with the 2D simulations (Figure 1b). It is evident that the topology of the structures significantly influences the distribution of hotspots with the edges, despite the significant rounding, guiding the plasmon formation. This is manifested: (i) in two hotspot areas for the concentric triangle, extending up and down and aligned with the edges of the center triangle column; (ii) small, localized hotspots in the center column of the concentric square and (iii) uniformly distributed hotspots across the whole cavity in the concentric hexagonal structure, which has the most uniform and closely packed edges and the highest degree of symmetry. To note, the field enhancement at the corners is not visible in square and hexagonal structures on the outer walls. Therefore, the formation of the hotspots in the edges of the center column, particularly for the square structure, is not just an edge effect. It is a consequence of the concentric structure and the cavity, further highlighting the enhanced SERS performance of coaxial topologies. For the 830 nm excitation laser, the strongest enhancement occurs between the tip and wedge in the gap toward the right and plasmonic enhancement is observed to propagate along the 60° side cavities. Overall, varying the gap distance width leads to the formation of a plasmon mode inside the coaxial structures' cavity, with the E_f excited on the gold micronano-structures initially increasing with decreasing gap-to-width ratios. While the periodic grating couples light into plasmon polariton and propagating plasmon resonances by diffraction, these are noted to couple with each other if the gap between the structures is large. The coupling for smaller gaps leads to increased localization between the architecture with increased E_f and, thus, higher SERS enhancements in the gaps. The increase in SERS with decreased interstitial gap due to resonant excitation of propagating plasmons diffractively coupled into the structure can be excited with the various laser wavelengths, depending on the cavity width. However, a considerable shrinking of the interstitial gap results in almost a complete elimination of the cavity plasmon mode with no manifestable resonance.

Subsequent to the numerical modeling, eXTRA fast maskless lithography with parallel multi-beam writing, speed up to 280 mm^2/min and resolution down to 300 nm was employed to fabricate high precision and throughput platforms. While the fabrication builds upon the numerical simulations and CAD designs to guide the optimal structures, the lithographic route enables the ease with which these could be scaled and tuned isotropically. Therefore, during the fabrication stages, it is possible to rapidly attain other desirable dimensions, rendering fabrication flexibility a key part in the design and iterations. The structures' up- and down scalability and tunability enabled us to further optimize the fabrication dimensions for optimal signal enhancement via isotopically scaling dimensions. The simulations were carried out for x and y polarized incident waves and the maximum value of the field on the surface of the structure was taken. When the structures are downscaled, the maximum field enhancement oscillates (Figure 2g), from a 27% lower value than the original scaling up to a 43.5% improvement. This is due to constructive and destructive interference of the plasmon resonance occurring in the structure and either the former or the latter dominating at different dimensions. This could be beneficial in further scaling the design structures to achieve a higher EF for a given polarization. The different dimensions resulting from the scaling of the structures affect the surface plasmon resonance and the constructive interference will be a valuable parameter for directing the fabrication of future features when scaling for y-polarized excitation. A scaling factor (a number ratio by which the fabricated structure dimension can be changed with respect to its original size) of × 0.56 was identified to exhibit an increased enhancement for both x and y incident polarization waves. This produced the highest Raman signals with a nearly twofold increase in enhancement relative to the original hollow concentric hexagonal architecture. The simulation and scalability optimization led to the fabrication of a range of optimal structured surfaces for the projected highest SERS enhancement (Figure S1, Supporting Information). These included concentric hexagons with outer and inner radii R_o = 3000 nm and R_i = 750 nm, respectively and wall width, w = 1.35μm (Figure 2a) generating an inner gap size of 650 nm as well as concentric rectangles and triangles with wall widths of w = 800 nm and w = 750 nm, respectively (Figure 2b,c). The substrates were typically arranged in 15 × 12 periodic arrays with a fixed period of 30 μm. The waveguide approximation provides further useful insights for a circular coaxial waveguide filled with air in the gap with the cutoff wavelength expressed as $\lambda = \pi(R_o+R_i)$, where R_o and R_i are the radii of the outer and inner surfaces.[62] With the latter being on the order of 1μm for the studied structures, the cutoff wavelength is $\lambda \approx$6μm. This is well above the maximum wavelength used for excitation, suggesting that the field can couple and propagate inside the structures, exciting the cavities.

The fabricated topological substrates were characterized via an array of optical (**Figure** 3a–c), scanning electron (Figure 3d–f) and atomic force (Figure 3g–i) microscopy (OM), (SEM), and (AFM), respectively.

To evaluate the SERS performance of the concentric patterned structures shown in Figure 3, these were coated with 30±12 nm thick gold layer (Figures S2 and S3, Supporting Information), followed by adsorption of a benzenethiol monolayer via immersing the gold-coated surfaces in 10 mM ethanolic solution. Representative average SERS spectra recorded for these metallic structures are shown in **Figure** 4b. The hexagonal and triangular hollow concentric structures produce better signal enhancement compared to their solid counterparts. Particularly, the hexagonal structures are found to be more effective in creating hotspots due to their

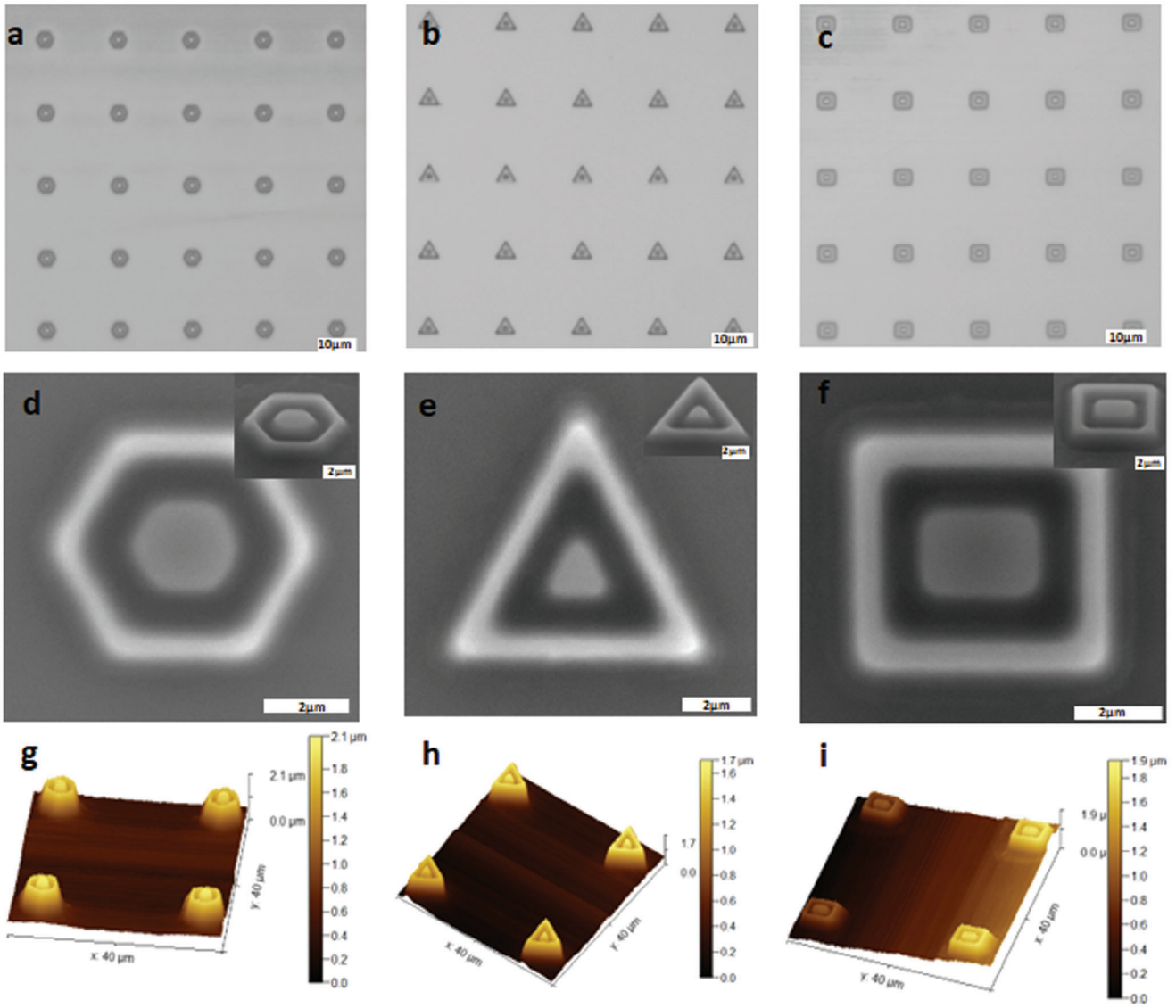

Figure 3. Representative OM top (a–c) and SEM (with 3D inset) (d–f) images of pattern formation, generating a range of SERS-active substrates including the hexagonal (a,d), triangular (b,e), and rectangular (c,f) structures with the corresponding 3D AFM height images (g–i).

six vertices and edges on the substrate surfaces. A similar, albeit to a lower degree, phenomenon was observed in the hollow concentric triangular structures with the regularity of the pattern allowing for the optimization of the SERS enhancement by controlling the size and spacing of the hotspots. By changing the arrangement of apertures from rectangular to triangular lattice, a more uniform mode resonance is formed in the plasmonic structures. This is due to the hollow concentric structures with sharp edges and crevices concentrating the target analyte molecules in the larger hotspot areas, yielding an effective Raman signal enhancement. These findings are in correspondence with previous studies, where the sharp corners and edges were found to exhibit stronger localized surface plasmon resonance (LSPR).[39,61,63]

Further to the averaged spectroscopic data, SERS mapping was carried out for each array. The representative SERS map overlaid over the corresponding optical microscopy images in Figure 4a shows the SERS signals arising exclusively from the concentric structures and no signal was observed from the flat gold-coated areas. This indicates that the adjacent structures are not plasmonically coupled and, therefore, can function as isolated detection centers, rendering these substrates as possible platforms for multiplexed SERS of diverse biochemical analytes.

Different morphologies were found to yield substantial variations in SERS enhancements (Figure 4b). The concentric hexagonal structures showed a 21 × enhancement compared to coaxial square arrays and a 12–15-fold increase in signal over the triangle structure at an excitation wavelength of 633 nm (Figure 4a). The absolute enhancement for the concentric hexagons was ≈1.2×10^6 at 633 nm and 3.9×10^5 at 785 nm. The 95% confidence intervals were (8.40×10^5, 1.30×10^6) and (3.0×10^5, 3.96×10^5), respectively. An EF of 0.8×10^5 with a 0.95 confidence interval of (0.75×10^5, 0.84×10^5) was found for the hollow

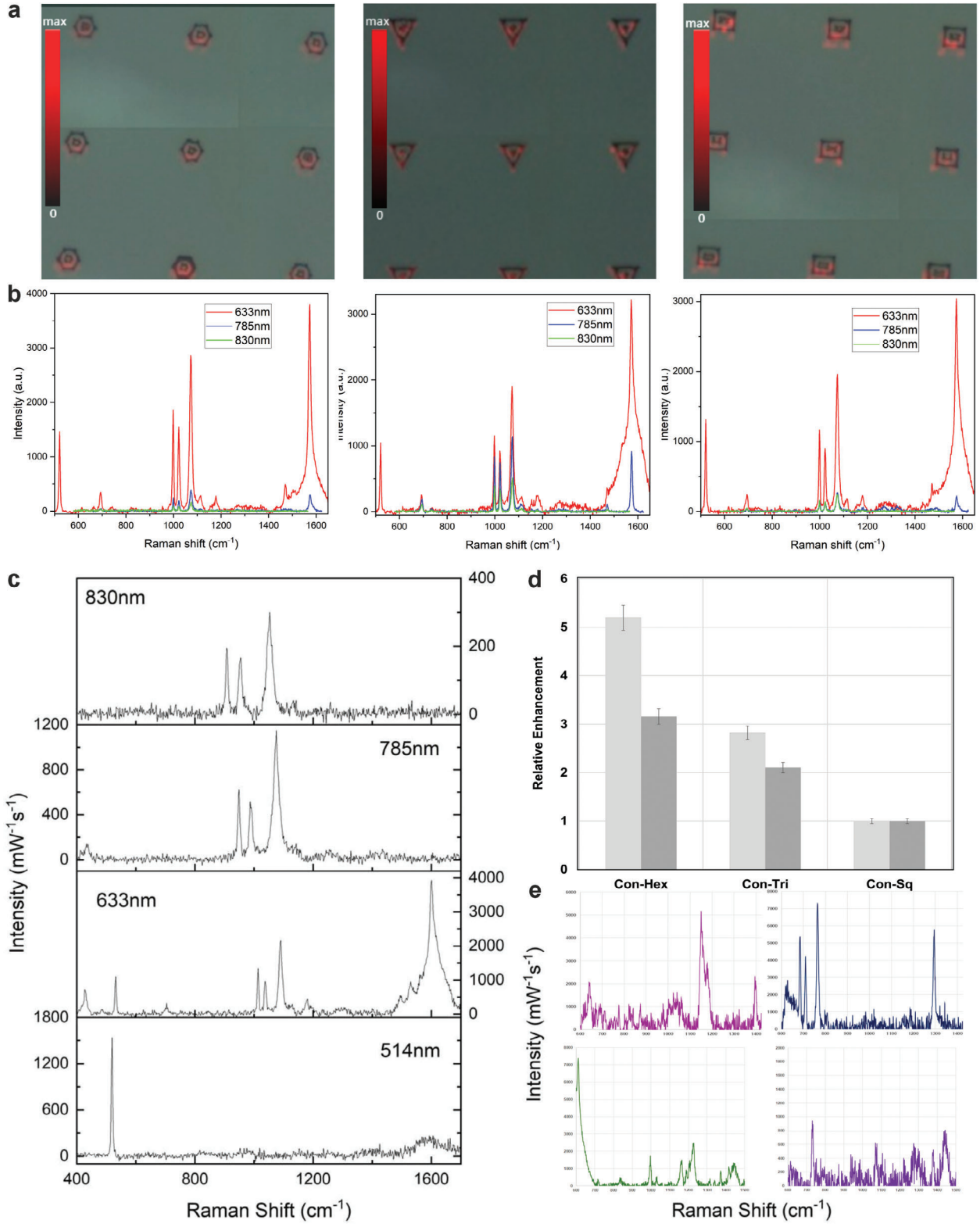

Figure 4. a) SERS maps overlaid over an optical image of the patterned area, revealing the localized nature of the SERS activity extracted for the benzenethiol peak at 1070cm^{-1}. b) SERS spectra of benzenethiol recorded from the three structured surfaces excited with 633, 785, and 830 nm lasers. c) SERS enhancement as a function of excitation wavelengths with the highest signal enhancement obtained for the hexagonal concentric structures with 633 nm followed by 785, 830, and 514 nm. d) Relative SERS enhancement of the 1000 cm^{-1} and 1070 cm^{-1} peaks for each concentric micro- nano topology. e) Average SERS spectra of representative TBI biomarker's fingerprint, including the sphingomyelin (purple), cholesterol (plum), myoinositol (green), and S100B (navy) deposited on hollow hexagonal coaxial SERS-active substrates and excited with a 785 nm laser.

coaxial triangular structures at 633 nm. The hollow concentric SERS structures were found to exhibit up to three times higher EFs than the solid equivalents due to the confined areas resulting in stronger local fields and larger surface area-to-volume ratio. The latter contributes to a larger number of the SERS-active molecules within the proximity of the plasmonic field, enhancing the Raman signal.

For a given micro- nanostructure, when an additional inner or outer similar architecture is added to make a concentric topology, it enables a larger bandwidth of electric field enhancement. This is due to a second resonance arising from the interaction of the inner and outer structural units, yielding a higher overall SERS enhancement. For all three fabricated topologies, the relative SERS enhancement of benzenethiol molecules was found to be the highest for the 633 nm excitation laser versus the 785 nm, with the 830 nm and the 514 nm excitations yielding negligible signal enhancement. Furthermore, the coaxial hexagonal SERS surface demonstrated the biggest increase in enhancement using the 633 nm excitation laser versus the 785 nm, exceeding the other two substrates. However, the concentric triangle surfaces exhibited the highest EF at 785 nm, × 3.3 and × 4.2 higher relative to the hexagonal and square morphologies, respectively, with the latter showing the lowest EF amongst the fabricated substrates (1.2×10^6 compared to 9.0×10^4) (Figure 4b–d).

Fluorescence was found to be significantly reduced in the spectra for all the excitation wavelengths except the 514 nm. The 785 and the 830 nm are typically preferred excitation lasers for biomedical applications, yielding reduced sample damage due to the lower photon energy.[64–68] The ultimate choice of excitation wavelength is often dictated by the plasmonic properties of the SERS substrates (or vice versa) as well as the analytes' resonance if a narrow range of compounds or similar physiological bodies are being targeted.[69–71] Since the SERS enhancement is dependent on the λ_i, mainly arising from the LSPRs of the metallic architectures, a particular substrate can yield the highest electromagnetic enhancement at a specified excitation. It is also strongly dependent on the surface morphology and precise shape of the features at the metal surface. Our results indicate that the hexagonal topology is the optimal structure to be exploited with the 633 nm excitation laser to yield the highest enhancement. Whereas the coaxial triangular morphology presents itself as a promising and viable candidate as an enhancing substrate with the 785 nm laser. The fabricated SERS-active substrates were subsequently used to profile four representative biomarkers signposted to correlate with TBI, successfully yielding the fingerprint spectra of sphingomyelin, cholesterol, myoinositol and S100B, characterizing the enhanced characteristic peaks of each biomarker (Figure 4e).

The experimental data was found to correspond with the numerical modeling, with the hexagonal coaxial structures providing the highest field enhancement across nearly all excitation wavelengths and concentric structures yielding higher enhancement compared to their solid counterparts. In comparison to results based on the fabricated substrates, higher enhancement factors are found for the ideal models based on simulations and CAD designs. This is attributed to neglecting minor fabrication imperfections such as inclined walls or minute depth variations. Furthermore, while the concentric triangular structures exhibited the highest enhancement in the ideal models, these are highly sensitive to topological deformations of the tip and the wedge. Whereas the concentric hexagons, with no similar tip, are less sensitive to defects and, thus, perform better experimentally than the modeled counterparts. This could further be considered in conjunction with the effects of tip-enhanced Raman spectroscopy (TERS), which combines SERS with scanning probe microscopy such as the AFM. TERS decouples molecular adsorption and enhancing processes, and the tip serves as an external enhancer. Localized surface plasmons can also be excited in the tip apex, providing a high near-field enhancement. Via theoretical simulations confirmed by the experimental investigations, the field enhancement properties of TERS have shown that plasmon coupling effects between the metal tip and the metal substrate play the key role in field enhancement, and the latter drops dramatically as the distance between the tip and the substrate increases. The spatial resolution was found to mainly be dependent on the radius of curvature of the tip end, with a sharp tip dramatically increasing the spatial resolution.[72–76] Correlation with the experiment could further be improved by applying a Gaussian beam as excitation instead of the plane wave, which is also more applicable for a small spot size. However, this is computationally unfeasible and therefore, symmetries could not be implemented to reduce the simulation domain.

From analysis of the coaxial geometries, it is noticeable from the simulation and the experimental outputs that when the topology of the designed structures is altered from square to triangle lattice, the plasmonic resonance modes are more uniform propagating along the 60° directions. This not only implies that the side-to-side, side-to-corner, and corner-to-corner resonance modes play key roles in light reflectance, but also indicates that the SERS signal can be tailor-enhanced by changing the arrangement of arrays from square to triangle lattice.

3. Conclusions

In conclusion, a range of coaxial topologically designed and optimized micro- and nanostructured substrates have been engineered as reproducible and tunable arrays for SERS. The morphologies were simulated via 2D and 3D near-field electric field distributions, revealing the predominant localization of the enhanced electromagnetic fields within the noble metal micro-nanostructures. In the coaxial geometries, the cutoff wavelength is found to be governed by the gap size and diameter of the structures. The tunable resonance available in these architectures couples and stores a significant amount of optical energy in the generated concentric cavities. Since the resonance wavelength independently of the cavity length dramatically red-shifts as a function of the gap size, this can enable a further construction of large-area arrays with $\lambda_{\text{resonance}} <<$period. The fabricated substrates were subsequently validated for the detection of a range of neurological biomarkers, exhibiting an average signal enhancement of $\times 10^6$. The fabricated concentric hexagonal, triangular, and rectangular morphologies with a broader bandwidth, a larger surface area and hot spots, increasing the molecular interactions in each region, show structure-dependent SERS performance. The structural and fabrication tunability allows the lithographically defined substrates to be optimized for plasmon-dependent phenomena. The ease of fabrication enables the micro nanostructures to be isotopically scaled up or down to the desired

topological dimensions whilst various micronano-architectures can be fabricated on the same substrate simultaneously. This enables to tailor-make specific topologies to achieve the optimal signal enhancement compatible with the chosen excitation wavelength. SERS enhancement requires a delicate balance between the excited and scattered wavelengths with the plasmon peak of the metallic micro-nanostructure. The plasmons excited at the scattered wavelength out-couple the Raman scattered radiation more efficiently. This is particularly important in the near-infrared, where the laser excitation and the scattered radiation can be significantly different in terms of wavelength. A range of SERS applicable laser excitation wavelengths, including the 514, 633, 785, and 830 nm, were applied for each fabricated substrate. The highest signal enhancement is found to arise from the hexagonal concentric micro-nanostructures with a 633 nm excitation laser, considerably outperforming the 514 nm and highlighting the consideration to be given to the choice of the excitation laser to detect the target bio-analytes. In the long-term, the fabrication of optimized concentric plasmonic micro- and nanostructured substrates with inherent tunability opens avenues for a strong analytical platform. These can be suitable for a range of applications, for instance, multiplexed detection of trace level disease indicative biomarkers, photocatalysis, environmental and forensic *on-site* detection, as well as miniaturized integrative sensing platforms.

4. Experimental Section

Materials: Silicon (Si) wafers (*n*-type, crystal orientation <100>) with a polished side and resistivity of 0–100 ohm-cm (WaferNet, GmbH Germany) were used as an underlying surface during substrate fabrication, acting as the base for the deposition of photoresists. HPLC-grade ethanol (Sigma-Aldrich) was used for the preparation of 10 mM Benzenethiol (BT) solution.[27,29]

SERS Substrates Fabrication: The positive and negative photoresists for the fabrication included AZ1514H and AZnLOF2020 (MicroChemicals, GmbH Germany), used without further dilution. Si wafers were initially thoroughly cleaned via physical techniques, including snow-jet, removing 99.99% of contaminants.[77] The photoresists (20 µL) were subsequently deposited on the clean Si wafers via spin-coating (Laurell, WS-650MZ-23NPPB) at 4 000 rotations per minute (rpm) for 60 s in a controlled humidity environment. Subsequently, photoresist-coated substrates underwent a softbake process to improve the adhesion of the photoresist to the wafer. This included heating at 100 °C for 90 s for a film thickness of 1.5 µm (1 min/µm resist film thickness) for the positive photoresist AZ1514H and 60 s for a film thickness of 2 µm for the negative photoresist AZnLOF2020. A range of micro and nanostructures were fabricated via a direct laser writer (model: Picomaster XF, brand: Raith) eXTRA fast maskless lithography system using a 405 nm laser. The eXTRA maskless lithography was operated in a vector writing mode performance to avoid stitching problems and optimize the depth of focus, laterally fabricating each surface. The established engineering of SERS platforms via eXTRA lithography in a single laser writing, for patterning the selected structures and dimensions, the optimal grid array organization included 15 and 12 structures in each line and row, respectively. This grid array of 15 × 12 ensured the optimal structural dimensions, optimal speed of patterning and spacing between the structures, maximizing both the capacity to enhance signal as well as ease and cost-effectiveness of the fabrication. For the negative photoresist, a post-exposure bake was necessary to complete the photoreaction initiated during exposure, prior to development, where, for the positive resist the exposed areas were dissolved using the AZ351B (MicroChemicals, GmbH Germany) and deionized water at 1:4 ratio (developer: water v/v)[78] and for the negative resist, the unexposed areas were removed using the AZ326MiF developer (MicroChemicals, GmbH Germany). The dissolution of the exposed areas was based on the conversion of the diazo naphthoquinone-sulphonate-based photoinitiator in indene carboxylic acid. The dilution of the AZ351B in water occurs due to the rate of dissolution of the exposed resist to the rate of dissolution of the unexposed resist, which remains on the substrate as the nanostructure.[78] The fabricated nanostructures were sputter-coated with a thin gold layer.

Optical Microscopy: Images of the fabricated nanostructures were acquired using Olympus Optical Microscope (GX61, GX2) with a Leica DM2700 M camera.

Scanning Electron Microscopy: The scanning electron microscopy (SEM) measurements were performed using a Hitachi SU5000 at acceleration voltages of 0.5-5KV with a lateral resolution of 2–5 nm.

Atomic Force Microscopy: The atomic force microscopy (AFM) measurements were performed using JPK NanoWizard II atomic force microscope. The measurements were done using tapping mode via an intermittent contact mode of the cantilever tip with the sample in ambient conditions. NCHV-A cantilevers with a resonance of 320 kHz and stiffness of 42Nm^{-1} were used. The software used to analyze the height and phase of the images was Gwyddion, version 2.59. The size of the nanostructures was measured by scanning 50 × 50µm^2 of each sample, with the regions chosen to represent different topologies obtained during fabrication.

SERS Acquisition: SERS measurements were carried out using micro-Raman system via an *inVia* Qontor confocal Raman spectrometer (Renishaw Plc) and four excitation lasers, including the 514, 633, 785, and 830 nm. To avoid photochemical effects, degradation or sample damage, SERS maps spectral scans were typically acquired for 100 data points over a range of 500–2000cm^{-1} with the laser power of 30–40 mW, 50x objective lens, the numerical aperture of 0.75, the acquisition time of 0.1s with 3 accumulations. All Raman spectra were collected at the ambient temperature. SERS enhancement factor (EF) of the fabricated structures was calculated via the: $EF = [I_{SERS}/N_{SERS}]/[I_{Normal}/N_{Normal}]$, where I_{Normal} is the intensity of the Raman scattering peak, I_{SERS} is the signal of the SERS substrate containing the fabricated structures, N_{SERS} and N_{Normal} are the numbers of adsorbed molecules on SERS active substrates with the surface density of the molecules taken as 3.3molecules/nm and the number of molecules probed for a normal Raman setting, respectively.[30]

Numerical Modeling: The computational simulations were conducted using the finite-element solver COMSOL Multiphysics 5.5,[79] with the Wave Optics module and frequency domain study. The topologies were modeled based on images in Fusion 360 and imported into COMSOL via CAD module. The silica substrate had a refractive index $n = 1.45$, the structure, which was made of photoresist, had a refractive index of $n = 1.58$, the top layer was air with $n = 1$, and the thin gold layer was modeled using transition boundary conditions with thickness $t = 40$ nm and gold permittivity from Johnson and Christy.[80] The excitation at each of the employed laser wavelengths was taken as a plane wave, with wavelength λ propagating along the *z*-axis (Figure 1). Separate *x* and *y* polarized wave studies were conducted. A mesh size of $\lambda/5$ was used. The symmetry of the structures was taken into account to reduce the computational domain, which was truncated approximately one λ from the structure and surrounded with scattering boundary conditions.

Supporting Information

Supporting Information is available from the Wiley Online Library or from the author.

Acknowledgements

The authors acknowledge funding from the Wellcome Trust (Grant No. 174ISSFPP) and the Engineering and Physical Science Research Council (Grant Refs: EP/V029983/1 and EP/L016346/1). The authors also acknowledge the EPSRC Centre for Doctoral Training in Topological Design. The authors further thank Dr Zoltan Sztranyovszky for his important inputs into this study.

Conflict of Interest

The authors declare no conflict of interest.

Data Availability Statement

The data that support the findings of this study are available from the corresponding author upon reasonable request.

Keywords

concentric substrates, micro/nano topographical structures, surface-enhanced raman spectroscopy (SERS)

Received: April 24, 2024
Revised: August 24, 2024
Published online:

[1] S. Nie, S. R. Emory, *Science* **1997**, *275*, 1102.
[2] K. Kneipp, Y. Wang, H. Kneipp, L. T. Perelman, I. Itzkan, R. R. Dasari, M. S. Feld, *Phys. Rev. Lett.* **1997**, *78*, 1667.
[3] Y. Zhao, E. Berenschot, H. Jansen, N. Tas, J. Huskens, M. Elwenspoek, *Microelectron. Eng.* **2009**, *86*, 832.
[4] J. Li, P. Song, J. Zhao, K. Vaklinova, X. Zhao, Z. Li, Z. Qiu, Z. Wang, L.i Lin, M. Zhao, T. S. Herng, Y. Zuo, W. Jonhson, W. Yu, X. Hai, P. Lyu, H. Xu, H. Yang, C. Chen, S. J. Pennycook, J. Ding, J. Teng, A. H. Castro Neto, K. S. Novoselov, J. Lu, *Nat. Mater.* **2021**, *20*, 181.
[5] A. Chandra, P. E. Valkimadi, G. Pagano, O. Cousins, G. Dervenoulas, M. Politis, *Human Brain Mapping*, Vol. *40*, John Wiley & Sons Ltd., Hoboken, NJ **2019**, pp. 5424.
[6] V. Brasiliense, J. E. Park, E. J. Berns, R. P. Van Duyne, M. Mrksich, *Sci. Rep.* **2022**, *12*, 1.
[7] O. Lyandres, N. C. Shah, C. R. Yonzon, J. T. Walsh, M. R. Glucksberg, R. P. Van Duyne, *Anal. Chem.* **2005**, *77*, 6134.
[8] P. Candeloro, E. Iuele, G. Perozziello, M. L. Coluccio, F. Gentile, N. Malara, V. Mollace, E. Di Fabrizio, *Microelectron. Eng.* **2017**, *175*, 30.
[9] S. Hanif, H.-L. Liu, S. A. Ahmed, J.-M. Yang, Y. Zhou, J. Pang, L.i-N.a Ji, X.-H. Xia, K. Wang, *Anal. Chem.* **2017**, *89*, 9911.
[10] D. K. Lim, K. S. Jeon, H. M. Kim, J. M. Nam, Y. D. Suh, *Nat. Mater.* **2010**, *9*, 60.
[11] P. Wang, M. Xia, O. Liang, K.e Sun, A. F. Cipriano, T. Schroeder, H. Liu, Y.a-H. Xie, *Anal. Chem.* **2015**, *87*, 10255.
[12] L. Wang, et al., *Anal. Chem.* **2019**, *91*, 6507.
[13] C. Leng, C. Wang, H. Xiu, X. Qu, L. Chen, Q. Tang, L.i Li, *Chin. J. Chem.* **2016**, *34*, 273.
[14] C. Srichan, M. Ekpanyapong, M. Horprathum, P. Eiamchai, N. Nuntawong, D. Phokharatkul, P. Danvirutai, E. Bohez, A. Wisitsoraat, A. Tuantranont, *Sci. Rep.* **2016**, *6*, 1.
[15] L. A. Wu, W. E. Li, D. Z. Lin, Y. F. Chen, *Sci. Rep.* **2017**, *7*, 1.
[16] D. Liu, C. Li, F. Zhou, T. Zhang, H. Zhang, X. Li, G. Duan, W. Cai, Y. Li, *Sci. Rep.* **2015**, *5*, 1.
[17] M. Navas-Moreno, M. Mehrpouyan, T. Chernenko, D. Candas, M. Fan, J. J. Li, M. Yan, J. W. Chan, *Sci. Rep.* **2017**, *7*, 1.
[18] Y. Wang, P. Zhao, L. Mao, Y. Hou, D. Li, *RSC Adv.* **2018**, *8*, 3143.
[19] T. Lee, G.a H. Kim, S. M. Kim, K. Hong, Y. Kim, C. Park, H. Sohn, J. Min, *Colloids Surf., B* **2019**, *182*, 110341.
[20] J. N. Anker, W. P. Hall, O. Lyandres, N. C. Shah, J. Zhao, R. P. Van Duyne, *Biosensing with plasmonic nanosensors*, Vol. *7*, Nature Publishing Group, New York **2008**, pp. 442.
[21] C. G. Khoury, T. Vo-Dinh, *J. Phys. Chem. C* **2012**, *116*, 7534.
[22] P. Goldberg-Oppenheimer, S. Mahajan, U. Steiner, *Adv. Mater.* **2012**, *24*, OP175.
[23] R. Kwak, H. E. Jeong, K. Y. Suh, *Small* **2009**, *5*, 790.
[24] Y. Zhao, E. Berenschot, M. de Boer, H. Jansen, N. Tas, J. Huskens, M. Elwenspoek, *J. Micromech. Microeng.* **2008**, *18*, 064013.
[25] C. Acikgoz, M. A. Hempenius, J. Huskens, G. J. Vancso, *Eur. Polym. J.* **2011**, *47*, 2033.
[26] C. L. Cheung, R. J. Nikolić, C. E. Reinhardt, T. F. Wang, *Nanotechnology* **2006**, *17*, 1339.
[27] K. Stokes, K. Clark, D. Odetade, M. Hardy, P. G. Oppenheimer, *Discov. Nano* **2023**, *18*, 153.
[28] H. Sharma, D. Nguyen, A. Chen, V. Lew, M. Khine, *Ann. Biomed. Eng.* **2011**, *39*, 1313.
[29] N. A. Abu Hatab, J. M. Oran, M. J. Sepaniak, *ACS Nano* **2008**, *2*, 377.
[30] A. Dhawan, Y. Du, F. Yan, M. D. Gerhold, V. Misra, T. Vo-Dinh, *IEEE Sens. J.* **2010**, *10*, 608.
[31] L. Petti, R. Capasso, M. Rippa, M. Pannico, P. La Manna, G. Peluso, A. Calarco, E. Bobeico, P. Musto, *Vib. Spectrosc.* **2016**, *82*, 22.
[32] B. X. E. Desbiolles, A. Bertsch, P. Renaud, *Microsyst. Nanoeng.* **2019**, *5*, 11.
[33] P. L. Stiles, J. A. Dieringer, N. C. Shah, R. P. Van Duyne, *Annu. Rev. Anal. Chem.* **2008**, *1*, 601.
[34] M. Moskovits, *J. Raman Spectrosc.* **2005**, *36*, 485.
[35] M. Gambucci, E. Cambiotti, P. Sassi, L. Latterini, *Molecules* **2020**, *25*, 3405.
[36] K. Kneipp, H. Kneipp, J. Kneipp, *Acc. Chem. Res.* **2006**, *39*, 443.
[37] M. Li, S. K. Cushing, N. Wu, *Analyst* **2015**, *140*, 386.
[38] M. A. Shenashen, S. A. El-Safty, E. A. Elshehy, *Part. Part. Syst. Charact.* **2014**, *31*, 293.
[39] Y. Sun, Y. Xia, *Science* **2002**, *298*, 2176.
[40] T. H. Chow, N. Li, X. Bai, X. Zhuo, L. Shao, J. Wang, *Acc. Chem. Res.* **2019**, *52*, 2136.
[41] Y. Sun, *Nanoscale* **2010**, *2*, 1626.
[42] W. Yue, Y. Fan, T. Zhang, T. Gong, X. Long, Y. Luo, P. Gao, *Spectrochim. Acta, Part A* **2022**, *267*, 120582.
[43] M. Kahl, E. Voges, S. Kostrewa, C. Viets, W. Hill, *Sens. Actuators, B* **1998**, *51*, 285.
[44] M. Chirumamilla, A. Toma, A. Gopalakrishnan, G. Das, R. P. Zaccaria, R. Krahne, E. Rondanina, M. Leoncini, C. Liberale, F. De Angelis, E. Di Fabrizio, *Adv. Mater.* **2014**, *26*, 2353.
[45] M. Lafuente, P. Muñoz, E. J. W. Berenschot, R. M. Tiggelaar, A. Susarrey-Arce, S. G. Rodrigo, L. J. Kooijman, S. M. García-Blanco, R. Mallada, M. P. Pina, N. R. Tas, *Appl. Mater. Today* **2023**, *35*, 101929.
[46] A. Gopalakrishnan, M. Chirumamilla, F. De Angelis, A. Toma, R. P. Zaccaria, R. Krahne, *ACS Nano* **2014**, *8*, 7986.
[47] Y. Xue, F. Scaglione, F. Celegato, P. Denis, H.-J. Fecht, P. Rizzi, L. Battezzati, *Chem. Phys. Lett.* **2018**, *709*, 46.
[48] X. Song, H. Li, H. M. Al-Qadiri, M. Lin, *J. Food Meas. Charact.* **2013**, *7*, 107.
[49] B. Calis, M. Yilmaz, *Colloids Surf., A* **2021**, *622*, 126654.
[50] B.o-K. Chao, Y.i Xu, H.-C. Ho, P. Yiu, Y.i-C. Lai, C.-H. Shek, C.-H. Hsueh, *Sci. Rep.* **2017**, *7*, 1.
[51] X. Zong, R. Zhu, X. Guo, *Sci. Rep.* **2015**, *5*, 1.
[52] B. Fortuni, T. Inose, S. Uezono, S. Toyouchi, K. Umemoto, S. Sekine, Y. Fujita, M. Ricci, G. Lu, A. Masuhara, J. A. Hutchison, L. Latterini, H. Uji-i, *Chem. Commun.* **2017**, *53*, 11298.
[53] X. Qian, X.-H. Peng, D. O. Ansari, Q. Yin-Goen, G. Z. Chen, D. M. Shin, L. Yang, A. N. Young, M. D. Wang, S. Nie, *Nat. Biotechnol.* **2008**, *26*, 83.
[54] G. C. Messina, M. Malerba, P. Zilio, E. Miele, M. Dipalo, L. Ferrara, F. De Angelis, *Beilstein J. Nanotechnol.* **2015**, *6*, 492.
[55] L. A. Austin, M. A. MacKey, E. C. Dreaden, M. A. El-Sayed, *Arch. Toxicol.* **2014**, *88*, 1391.
[56] N. Schneider, J. Hauser, M. Oliveira, E. Cazaubon, S. C. Mottaz, B. V. O'Neill, P. Steiner, S. C. L. Deoni, *eNeuro* **2019**, *6*, 0421.

[57] H. Nishiyama, T. Knöpfel, S. Endo, S. Itohara, *Proc. Natl. Acad. Sci. U. S. A.* **2002**, *99*, 4037.
[58] J. M. Pascual, J. Solivera, R. Prieto, L. Barrios, P. López-Larrubia, S. Cerdán, J. M. Roda, *J. Neurotrauma* **2007**, *24*, 944.
[59] H. Xu, L.e-X. Zheng, X.-S. Chen, Q.-Y.u Pang, Y.a-N. Yan, R. Liu, H.-M.u Guo, Z.-Y. Ren, Y. Yang, Z.-Y.a Gu, C. Gao, Y. Gao, C.-L. Luo, Y. Zhao, Y. Wang, T. Wang, L.u-Y. Tao, *Brain Pathol.* **2023**, *33*, e13126.
[60] J. M. Park, H. E. Choi, D. Kudaibergen, J. H. Kim, K. S. Kim, *Front. Chem.* **2021**, *9*, 419.
[61] A. Genç, J. Patarroyo, J. Sancho-Parramon, N. G. Bastús, V. Puntes, J. Arbiol, *Nanophotonics* **2017**, *6*, 193.
[62] F. I. Baida, A. Belkhir, D. Van Labeke, O. Lamrous, *Phys. Rev. B* **2006**, *74*, 205419.
[63] C. R. Rekha, S. G. Jiji, V. U. Nayar, K. G. Gopchandran, *Vib. Spectrosc.* **2021**, *114*, 103233.
[64] C. M. Creely, G. Volpe, G. P. Singh, M. Soler, D. V. Petrov, *Opt. Exp.* **2005**, *13*, 6105.
[65] R. J. Swain, M. M. Stevens, in *Biochemical Society Transactions*, Portland Press, London **2007**, pp. 544–549.
[66] A. R. M. Radzol, K. Y. Lee, W. Mansor, S. R. Yahaya, in Procedia Engineering, No longer published by Elsevier, **2012**, pp. 867–873. https://doi.org/10.1016/j.proeng.2012.07.256.
[67] A. Zoladek, F. C. Pascut, P. Patel, I. Notingher, *J. Raman Spectrosc.* **2011**, *42*, 251.
[68] F. Draux, P. Jeannesson, A. Beljebbar, A. Tfayli, N. Fourre, M. Manfait, J. Sulé-Suso, G. D. Sockalingum, *Analyst* **2009**, *134*, 542.
[69] M. Hardy, L. Kelleher, P. de Carvalho Gomes, E. Buchan, H. O. M. Chu, P. Goldberg Oppenheimer, *Appl. Spectrosc. Rev.* **2022**, *57*, 177.
[70] Z. Movasaghi, S. Rehman, I. U. Rehman, *Appl. Spectrosc. Rev.* **2007**, *42*, 493.
[71] A. C. S. Talari, Z. Movasaghi, S. Rehman, I. U. Rehman, *Appl. Spectrosc. Rev.* **2015**, *50*, 46.
[72] G. Picardi, "Raman spectroscopy and light emission at metal surfaces enhanced by the optical near field of a scanning tunnelling tip," PhD Dissertation, **2003**, https://doi.org/10.17169/REFUBIUM-15803.
[73] Z. Yang, J. Aizpurua, H. Xu, *J. Raman Spectrosc.* **2009**, *40*, 1343.
[74] N. Hayazawa, Y. Inouye, Z. Sekkat, S. Kawata, *Opt. Commun.* **2000**, *183*, 333.
[75] B. Pettinger, B. Ren, G. Picardi, R. Schuster, G. Ertl, *Phys. Rev. Lett.* **2004**, *92*, 8.
[76] B. Ren, G. Picardi, B. Pettinger, R. Schuster, G. Ertl, *Angew. Chemie., Int. Ed.* **2004**, *44*, 139.
[77] R. Sherman, D. Hirt, R. Vane, *J. Vac. Sci. Technol. A* **1994**, *12*, 1876.
[78] M. C. GmbH, "Application Notes for photolithography with technical information for photoresists, solvents, developers and etchants.", https://www.microchemicals.com/downloads/application_notes.html (accessed: May 2022).
[79] COMSOL Multiphysics, "COMSOL – Software for Multiphysics Simulation," COMSOL Multiphysics/Heat Transfer Module, https://www.comsol.com/ (accessed: November 2023).
[80] P. B. Johnson, R. W. Christy, *Phys. Rev. B* **1972**, *6*, 4370.